Scintillation yield and time dependence from electronic and nuclear recoils in liquid neon

W. H. Lippincott,[1,2,*] K. J. Coakley,[3] D. Gastler,[4] E. Kearns,[4] D. N. McKinsey,[2] and J. A. Nikkel[2]
[1]*Fermi National Accelerator Laboratory, Batavia, Illinois 60510, USA*
[2]*Department of Physics, Yale University, New Haven, Connecticut 06511, USA*
[3]*National Institute of Standards and Technology, Boulder, Colorado 80305, USA*
[4]*Department of Physics, Boston University, Boston, Massachusetts 02215, USA*
(Received 9 November 2011; revised manuscript received 21 May 2012; published 18 July 2012)

We have performed measurements of scintillation light in liquid neon, observing a signal yield in our detector as high as (3.5 ± 0.4) photoelectrons/keV. We measure pulse shape discrimination efficiency between electronic and nuclear recoils in liquid neon from 50 to 300 keV nuclear recoil energy. We also measure the $\mathcal{L}_{\text{eff}}$ parameter in liquid neon between 30 and 370 keV nuclear recoil energy, observing an average $\mathcal{L}_{\text{eff}} = 0.24$ above 50 keV. We observe a dependence of the scintillation time distribution and signal yield on the pressure and temperature of the liquid neon.

DOI: 10.1103/PhysRevC.86.015807 PACS number(s): 29.40.Mc, 61.25.Bi, 25.40.Dn, 34.50.Gb

I. INTRODUCTION

The DEAP/CLEAN Collaboration has proposed using liquid argon and liquid neon as scintillating targets in large-scale detectors to observe both *pp* solar neutrinos and dark matter in the form of weakly interacting massive particles (WIMPs) [1–3]. In particular, the MiniCLEAN experiment is designed to do a dark matter search with first liquid argon and then liquid neon as both a systematic check on backgrounds and as a precursor to a multi-ton-scale detector [4]. Because of the expected A^2 dependence of the cross section for WIMP-nucleon scattering [5], filling the same detector alternately with argon and neon will change the expected dark matter signal in a known way while maintaining an identical level of external backgrounds. Here, we extend previous studies of the scintillation properties of liquid neon [6].

Like the other liquefied noble gases, liquid neon is relatively inexpensive, is easily purified of radioactive contaminants, scintillates brightly when exposed to ionizing radiation, and is dense enough to self-shield, reducing the background level in the center of a larger volume of liquid. The key for dark matter detection is to be able to suppress the electronic recoils that make up most of the backgrounds from the nuclear recoils that would make up a WIMP signal by use of some combination of self-shielding and discrimination. Because ν_e-e scattering also produces electronic recoils, discrimination does not improve the performance of a neutrino detector. However, neon has no long-lived radioactive isotopes and is more readily purified of contaminants such as ^{39}Ar and ^{85}Kr [7] than the heavier noble gases, rendering it an ideal target for low-energy neutrinos.

When ionizing radiation interacts in liquid neon or any other liquefied noble gas, ultraviolet light is produced via scintillation. The incoming radiation collides with an electron or nucleus in the liquid and deposits energy. The resulting electronic or nuclear recoil then excites or ionizes other neon atoms. The excited atoms quickly combine with surrounding ground-state atoms to form dimer states, Ne_2^*. The ions also bond with ground-state atoms to form ionized molecules, Ne_2^+, which can in turn recombine with free electrons to also form the excited dimer states. Finally, the dimer states decay by emitting scintillation photons with a wavelength of 80 nm. Because these photons have insufficient energy to excite neon atoms [8], the liquid does not absorb its own scintillation light and large light yields can be attained from liquid noble gas detectors.

The metastable molecules are produced in both singlet and triplet states. The singlet state decays in nanoseconds, while the triplet state undergoes a forbidden spin flip before decaying, extending the triplet lifetime to 15 μs in neon [6]. Because nuclear and electronic recoils produce different ratios of singlets to triplets, pulse timing can be used to identify the source of the initial excitation via pulse shape discrimination (PSD) [2,3]. As the PSD depends directly on the scintillation timing, we have attempted to remeasure the time constants of liquid neon scintillation in this work. We discovered two additional time components in the light signals produced by ionizing radiation, and we also found that both the intensity and lifetime of each component change significantly with the temperature and pressure of the liquid, a new feature that is not observed in the heavier noble gases.

A second property of scintillation in liquefied noble gases is that nuclear recoils produce less light than electronic recoils of the same energy. The ratio of signal yields at zero electric field for the two event classes is known as the nuclear recoil scintillation efficiency, or $\mathcal{L}_{\text{eff}}$. The value of $\mathcal{L}_{\text{eff}}$ in combination with the discrimination efficiency sets the nuclear recoil energy analysis threshold of a liquefied noble gas dark matter detector. Because in general $\mathcal{L}_{\text{eff}} < 1$, two energy scales may be employed, denoted "keVee" and "keVr." The actual energy deposited by a nuclear recoil is expressed in units of keV recoil or keVr. Most calibration sources used in liquid noble gas detectors are γ or β sources that produce electronic recoils in the liquid. Therefore, the energy calibration gleaned from these sources refers to the energy deposited by an electronic recoil, or keV electron equivalent (keVee). In practice, we often have no direct energy calibration for nuclear recoils and so use electron equivalent

*hugh@fnal.gov

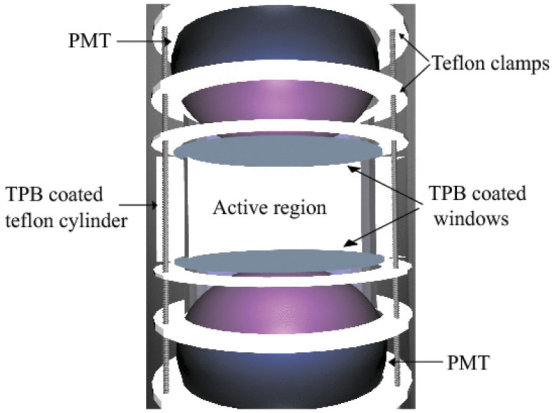

FIG. 1. (Color online) Schematic representation of the MicroCLEAN scintillation cell.

energies. The conversion factor is $\mathcal{L}_{\text{eff}}$. At zero electric field

$$E[\text{keVee}] = E[\text{keVr}] \times \mathcal{L}_{\text{eff}}. \quad (1)$$

Pulse shape discrimination has been studied in argon [9–11] and xenon [12–14]. Our group performed a measurement of PSD in neon as well, but nuclear recoils were observed at only one energy [6]. Similarly, $\mathcal{L}_{\text{eff}}$ has been measured in argon [15] and xenon [16–20], but at only one energy in neon. In this paper, we report measurements of scintillation light in liquid neon over a wide energy range. We measure PSD from 50 to 300 keVr and $\mathcal{L}_{\text{eff}}$ from 30 to 370 keVr. We also present results on the time dependence of liquid neon scintillation light as a function of temperature.

II. EXPERIMENTAL APPARATUS

The apparatus used in these measurements is named MicroCLEAN and has been described in detail elsewhere [9]. A schematic is shown in Fig. 1. The detector has an active volume of 3.14 l viewed by two 200-mm-diameter Hamamatsu R5912-02MOD photomultiplier tubes (PMTs), which are specifically designed for use in cryogenic liquids. The active volume is defined by a polytetrafluoroethylene (PTFE) cylinder, 200 mm in diameter and 100 mm in height, with two 3-mm-thick fused-silica windows at top and bottom. All inner surfaces of the PTFE and windows are coated with (0.20 ± 0.01) mg/cm^2 of tetraphenyl butadiene (TPB) [21], which shifts the wavelength of the ultraviolet light to approximately 440 nm. The TPB thickness on the PTFE cylinder was reduced by 33% relative to that used in [9] to mitigate TPB absorption of the wavelength-shifted light. The MicroCLEAN vessel is contained within a stainless steel vacuum dewar for thermal insulation purposes.

The gas handling system is shown schematically in Fig. 2. Ultra-high-purity neon flows through a Nupure Omni 1000 [22][1] getter and an external charcoal trap at 77 K (not shown)

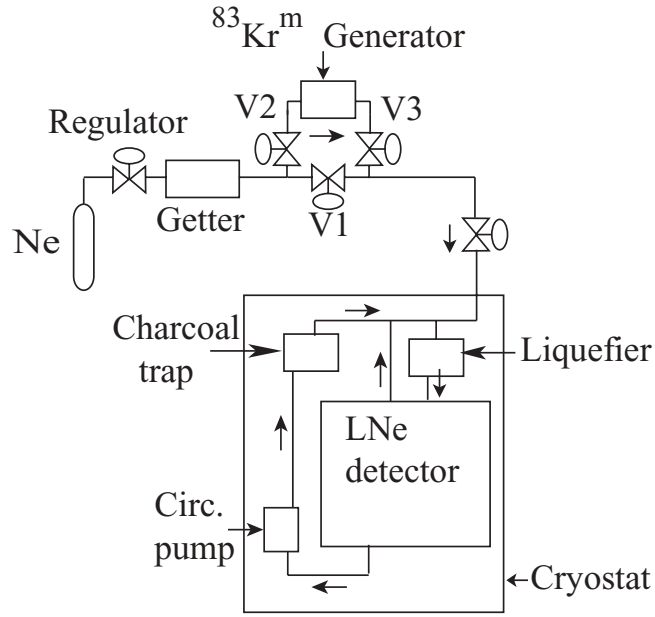

FIG. 2. The gas handling system for the MicroCLEAN runs described in this paper. The circulation pump consists of a heater that evaporates the liquid; the gas then flows through the charcoal trap before being reliquefied.

before passing into a vacuum cryostat through a tube at the top. Previous studies have shown that activated charcoal provides a very effective purifier of many impurities in neon, including radon [7]. Once inside the vacuum cryostat, the gas flows into a copper liquefier cell attached to the second stage of a Cryomech model PT805 cryorefrigerator before dripping into the MicroCLEAN vessel.

There is a circulation loop inside the vacuum dewar for continuous purification of the neon, again using activated charcoal as the purifier. Liquid neon flows out of the bottom of the MicroCLEAN vessel into a nearby plumbing volume containing a heater. The heater (labeled "Circ. pump" in Fig. 2) acts as a pump by boiling the liquid; the resulting pressure differential between the heater and the liquefier drives gas up a tube through a charcoal trap mounted inside the cryostat before it reenters the top of the liquefier, where gravity pulls the liquid back into the main chamber.

The "^{83}Kr^{m} Generator" shown in Fig. 2 refers to the setup for introducing ^{83}Kr^{m} into the liquid neon for calibration purposes as described in Sec. II B and [23]. The ^{83}Kr^{m} generator is connected to the gas inlet line just outside the vacuum dewar. The incoming gas can be diverted through the trap on its way into the detector to introduce ^{83}Kr^{m} atoms into the neon.

A. Data acquisition and processing

The data acquisition (DAQ) system consists of a 250-MHz, 12-bit CAEN V1720 waveform digitizer (WFD). The two

[1]Commercial equipment, instruments, or materials are identified in this paper to adequately specify the experimental procedure. Such identification implies no recommendation or endorsement by NIST, nor does it imply that the materials or equipment identified are necessarily the best available for the purpose.

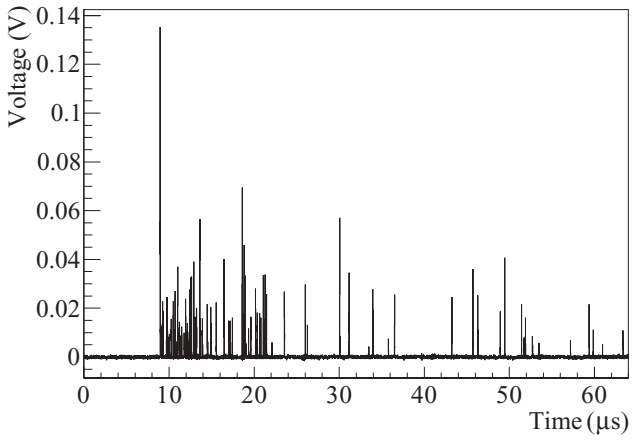

FIG. 3. Sample event from a single PMT digitized by the CAEN V1720 waveform digitizer. More than 8 μs of presamples are recorded to measure the baseline.

PMT channels are recorded with a record length of 64 μs to collect as much of the long-lived triplet light as possible, and a sample trace is shown in Fig. 3. The PMT signals are passed through a LeCroy model 612AM dual-output amplifier, with one copy passed to the WFD and the other copy sent to triggering electronics. The trigger is set in several different configurations. In most cases, a trigger is generated when each PMT signal crosses a threshold of 1/2 times the mean height of a single photoelectron within a 100-ns coincidence window. For some low-energy runs when an external detector is used as a coincidence tag, the trigger is generated when the sum of the two PMT signals crosses a threshold of roughly 1/2 the size of a photoelectron in coincidence with a signal in the external tagging detector. In each 64-μs data record, approximately 8 μs of presamples are collected to measure the baseline of each pulse. The data collected by the DAQ software are saved in a ROOT-based file structure for analysis [24].

The data processing is similar to that described in [9]. The presamples are averaged to obtain a baseline and a baseline root mean square, and the baseline is subtracted from each trace. We integrate each trace from 50 ns before the trigger (defined as the time at which the voltage first rises above 20% of its maximum value) to 44 μs after the trigger to determine the total area of each pulse. In performing this integral, we restrict the range of integration to 100-ns windows around locations where the trace voltage crosses a threshold of three times the baseline root mean square. This integration method is a hybrid of single-photoelectron counting and pulse integration. We reject data for which the trigger times of the two PMTs differ by greater than 20 ns. We define an asymmetry parameter,

$$A = \frac{S_T - S_B}{S_T + S_B}, \tag{2}$$

where S_T and S_B are the signal areas in the top and bottom PMTs. We reject data for which the asymmetry parameter is farther than 2σ from the mean value as determined by fitting a Gaussian function to the asymmetry data.

As the triplet component of liquid neon scintillation is spread out over tens of microseconds, there are many single-photoelectron pulses well separated in time in the tails of events. To obtain a single-photoelectron spectrum for each PMT, the last 30 μs of each trace is evenly divided into 150-ns windows. If the voltage spread in the first and last 30 ns of each 150 ns window is less than three times the size of the baseline root mean square, the peak height and pulse area of the window are collected in a two-dimensional histogram; this restriction prevents inclusion of partial single photoelectrons in the data set. A Gaussian is fit to the one-dimensional histogram of the pulse areas to determine the mean single-photoelectron size.

In previous tests of the R5912-02MOD, it was found that the gain dropped substantially at 30 K [25]. For the data presented here, we observe a sharp drop in PMT gain upon cooling to liquid neon temperatures, followed by a slow decrease in gain over several weeks before finally reaching a plateau. The low resulting gain necessitates the application of higher voltages to the PMTs and amplification from the LeCroy 610AM amplifier; for most of the data presented here, the PMTs are biased at 1750 V, the absolute gain of the PMTs is $\approx 1.1 \times 10^6$, and the PMT signals are further amplified by a factor of 10 with the LeCroy amplifier. A single photoelectron peak is resolved in the bottom PMT but not in the top PMT. To improve PMT performance, we use two high-voltage lines to bias the PMTs, with a separate high voltage running directly to the first dynode. By tuning the first dynode voltage relative to the total voltage, we can achieve some improvement in the single-photoelectron spectra but not enough to recover a resolvable single-photoelectron peak in the top PMT.

B. Radioactive sources

We use several radioactive sources for calibration purposes: the $^{83}Kr^m$ generator described in [23], a 10-μCi ^{22}Na source for 511- and 1275-keV γ rays, and a ^{2}H-^{2}H neutron generator ("D-D neutron generator") producing a monoenergetic beam of 2.8-MeV neutrons [26]. The $^{83}Kr^m$ generator produces metastable $^{83}Kr^m$ nuclei that decay via two electromagnetic transitions with energies of 32.1 and 9.4 keV. The second transition has a half-life of 154 ns, and given the long time scale of liquid neon scintillation, both transitions are observed together as a single waveform with a total energy of 41.5 keV. The ^{22}Na source produces positrons that immediately annihilate into two 511-keV γ rays with opposite momenta; we tag the second γ ray using a NaI crystal placed back-to-back with our apparatus to improve the data quality from the ^{22}Na source and reduce backgrounds. We reject data where the trigger times in the NaI crystal and the liquid neon differ by more than 30 ns, and we also make a cut to select events within 2σ of the 511-keV peak of the NaI crystal.

We also use a tagging detector when investigating nuclear recoils with the neutron generator. We require a PMT viewing BC501A organic scintillator to record an event within 200 ns of an event in the liquid neon. The organic scintillator is contained in a cylinder with a diameter of 127 mm and a depth of 127 mm. We also make a PSD cut in the organic scintillator and a cut on the time of flight (TOF) between the event in the liquid neon and the tagging detector. These cuts will be discussed in more detail in Sec. IV. Both the neutron generator and the organic scintillator are located approximately 1.63 m

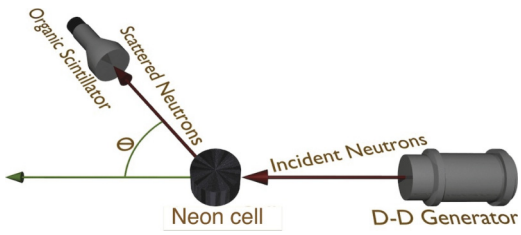

FIG. 4. (Color online) Schematic of the neutron scattering setup.

from MicroCLEAN, and the experimental setup can be seen schematically in Fig. 4. By changing the scattering angle θ, we can choose the energy of the nuclear recoils that scatter just once in the liquid, $E_{\rm rec}$, using simple kinematics:

$$E_{\rm rec} = \frac{2E_{\rm in}}{(1+M)^2}[1 + M - \cos^2(\theta) - \cos(\theta)\sqrt{M^2 + \cos^2(\theta) - 1}], \quad (3)$$

where $E_{\rm in}$ is the incident neutron energy and M is the atomic mass of the target. We measure the angle by running a string marked at both ends and at its midpoint from the generator around the dewar and back to the generator. We mark the location of the midpoint of the string on the dewar and then repeat the process for the organic scintillator. The ratio of the arc length between the two points on the dewar to the circumference (175.6 cm) provides the angle, θ. The accuracy is limited by our knowledge of the midpoint of the string, and by repeated measurements we estimate the uncertainty on the arc length to be 6.4 mm, for an uncertainty on the angle of 1.3°.

C. Energy calibration

We obtain an energy calibration by comparing ^{22}Na data with a simulation of the detector performed with the Reactor Analysis Tool (RAT) [27]. Combining GEANT4 and ROOT [24,28] in a single simulation package, the RAT simulation of MicroCLEAN contains a complete optical model of the inner detector and PMTs and has been used previously in studies of liquid argon scintillation [9,15]. In general, there are two features in the ^{22}Na data that can be used for calibration purposes: a 511-keV photoabsorption "hump" and the Compton edge.

The analysis begins by first obtaining a rough estimate for the signal yield from the 511-keV hump, without using the simulation. We tune the parameters of the simulation to achieve the estimated light yield before simulating the ^{22}Na source including a flat background contribution to account for the events observed above 600 keV from accidental coincidence of background events in the argon and 511-keV γ rays in the NaI detector. We then refit the data to the simulated spectrum, and the scale factor between the integrated charge from both PMTs to the energy scale of the simulation provides the energy calibration; an example of this fit is shown in Fig. 5. While the energy resolution is not an explicit parameter of the fit, we do smear the photon counts from the simulated spectrum with a Gaussian kernel having a standard deviation of $\sqrt{2 \times \langle N_{pe} \rangle}$, as this smearing provides better agreement between simulation and data. This additional smearing suggests a source of noise in the real experiment that is not being accurately modeled in the simulation, and a likely source of this noise is the poor gain dispersion characteristics of the PMTs. It could also be a property of the liquid neon.

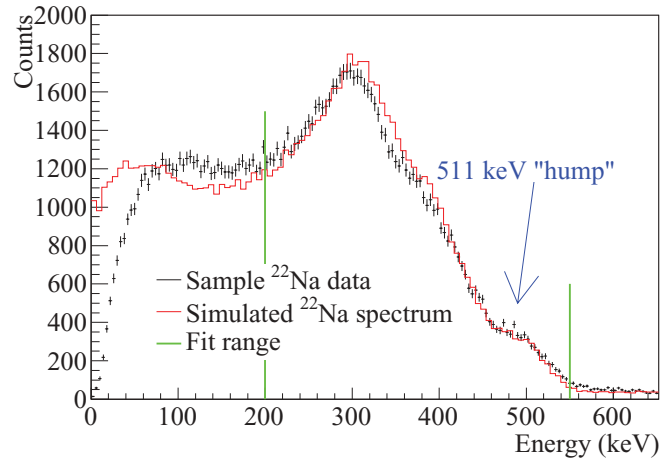

FIG. 5. (Color online) The energy calibration obtained by fitting the Compton edge and photoabsorption hump produced by 511-keV γ rays to a simulation of the detector. The green lines denote the fit range. We currently have no satisfactory explanation for the excess of events between 40 and 200 keV in comparing the data to the simulation.

The simulation does not accurately model the data below about 200 keV, predicting about 10% fewer counts than observed down to the low energies where thresholding effects begin (about 40 keV for the run shown in Fig. 5). This data excess is seen for a variety of different gain and trigger threshold settings, and it is currently unexplained, although asymmetry effects between the PMTs smearing out very low energy events is one possibility, as is an additional source of background in the detector. Given the discrepancy between data and simulation and the fact that the trigger and gain settings were varied throughout the course of the run, the energy calibration fit is performed between 200 and 550 keV.

There is some tension between the best fit at the Compton edge and the 511-keV hump, and the average χ^2/NDF is 2.5 for all runs with the nominal fit range (where NDF is number of degrees of freedom). If the fit is restricted to the range between 350 and 550 keV, the agreement is much better, with an average χ^2/NDF of 1.4. We estimate the systematic uncertainty caused by this tension to be 3% by fitting each feature independently and taking the difference in the resulting energy scale relative to the nominal fit as the uncertainty. Performing the fit without the flat background contribution in the simulation changes the calibration by less than 1%. An additional source of uncertainty in this calibration involves the statistics of fitting the simulated and observed spectra, but this source of uncertainty is estimated to be 1%.

We cross-check the energy calibration obtained from the ^{22}Na source with both higher and lower energy references. For our lower energy reference, we use the ^{83}Kr^{m} source described in the next section, which is the primary reason we believe the energy calibration is accurate to within our

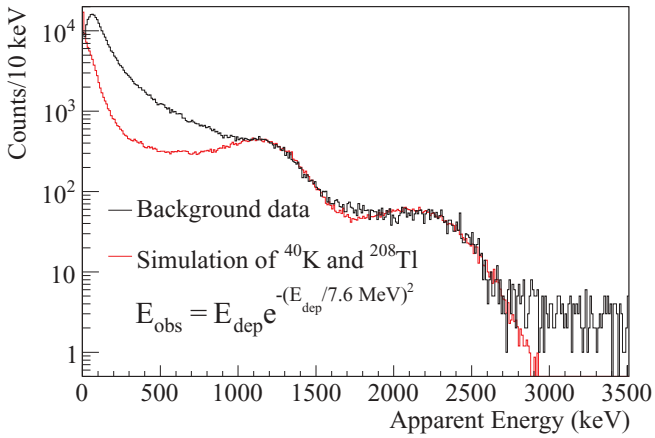

FIG. 6. (Color online) The energy calibration obtained from the ^{22}Na source checked by comparing background data to simulations containing ^{40}K and ^{208}Tl components. We clearly see the two Compton edges of the 1.4- and 2.6-MeV γ rays produced by these sources. We do not attempt to simulate any other backgrounds, so the divergence of data and Monte Carlo (MC) below 1000 keV is not surprising. There is evidence for a nonlinearity in the energy scale at these high energies that is likely related to the response of the top PMT, and we correct for this using Eq. (4).

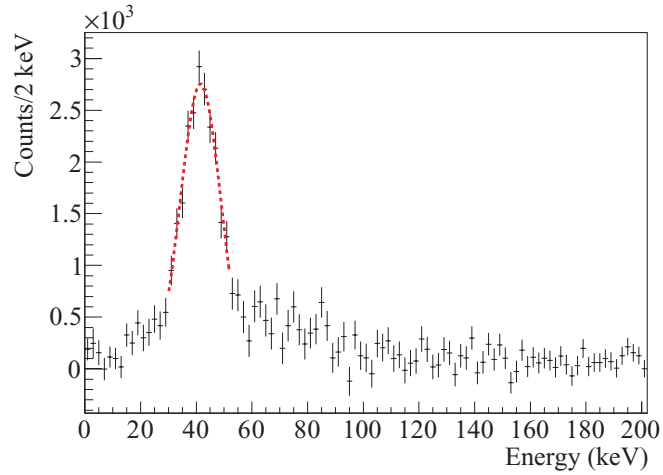

FIG. 7. (Color online) Energy spectrum of a background-subtracted ^{83}Kr^{m} run in neon. As discussed in the text, the observed light yield for these data is (3.0 ± 0.3) photoelectrons/keVee. The resolution is 19% (with σ/E of the Gaussian fit shown in red) at 41.5 keV.

uncertainties. For the higher energy reference, we look at the Compton edges of the 1.4- and 2.6-MeV γ rays produced in the decay of ^{40}K and ^{208}Tl, as there are a number of these events in the background data. Figure 6 shows the background data with the energy scale derived from the ^{22}Na calibration compared to a simulation of 1.4- and 2.6-MeV γ rays using the RAT simulation. As the purpose of this simulation is solely to cross-check the accuracy of the energy scale derived from the ^{22}Na at higher energies, we do not attempt to simulate any other sources of background (i.e., lower energy γ rays in the detector materials, cosmic rays, or other backgrounds); therefore, we do not expect the simulation to agree with the data below 1 MeV. We find evidence for a slight nonlinearity in either the energy response of the liquid neon or the PMTs at these energies, as the background data do not agree with the simulation if we assume a linear response of the detector up to 2.6 MeV. The fit is improved if the observed energy (as calibrated by the ^{22}Na source) is actually representing the following function of the deposited energy in the simulation:

$$\langle E_{\rm obs} \rangle = E_{\rm dep} \times e^{-(E_{\rm dep}/7.6\,{\rm MeV})^2}. \quad (4)$$

It is likely that this dependence is caused by a nonlinearity of the top PMT, as a comparison using just the signal in the bottom PMT requires no energy scaling to provide agreement. We also find that the data are best fit with an energy resolution of $\sigma = 2.4\sqrt{E_{\rm dep}}$. Between 1 and 2.7 MeV, we find a χ^2/NDF for this fit of 1.27.

D. The ^{83}Kr^{m} source

Previously, we reported on use of a ^{83}Kr^{m} generator as a source of low-energy electronic recoils in liquid argon and neon [23]. This Kr generator became available at the end of the experiment described here to provide a second, independent energy calibration at 41.5 keV, with a clear peak appearing in the data as shown in Fig. 7. When the energy calibration is derived from the ^{22}Na spectrum as described above, the energy of the ^{83}Kr^{m} peak agrees with 41.5 keV within statistical uncertainties, suggesting both that the energy calibration is accurate and that the response of the MicroCLEAN detector is linear between 9.4 and 511 keV. The resolution of our detector at 41.5 keV is 19% (σ/E of the Gaussian fit shown in Fig. 7).

E. Signal yield

The energy calibration described above uses the total signal from both PMTs. Given the absence of a well-defined mean single photoelectron in the top PMT, the absolute signal yield is estimated from the bottom PMT alone by matching the energy calibration to the integrated charge of the bottom PMT divided by the size of the single photoelectron of the bottom PMT. After ending the liquid neon run described in this report, we filled the detector with liquid argon without warming it up to room temperature or opening the system; at the higher temperatures of liquid argon, we were able to resolve the single-photoelectron response of both PMTs. From these measurements, we determined that the top tube observes (6 ± 3)% more signal than the bottom tube [23], due to some combination of photon collection efficiency and photocathode quantum efficiency. Therefore, we extrapolate the total light yield in the liquid neon to include both tubes based on the observed PMT efficiencies. Using this method, we determine a photoelectron yield of (3.0 ± 0.3) photoelectrons/keVee from the ^{83}Kr^{m} data. The total uncertainty includes an estimate of the uncertainty in the relative efficiency of the two tubes introduced by changing the temperature from 85 to 25 K, but it is dominated by the single-photoelectron response of the bottom PMT.

We next use the $^{83}Kr^{m}$ data to validate the ^{22}Na calibration method. By neglecting the systematic uncertainties from the PMT photoelectron response and efficiency, as they apply equally to both methods for determining the light yield, the standard ^{22}Na energy calibration taken at the same time as the $^{83}Kr^{m}$ data returns a light yield of (3.00 ± 0.02) photoelectrons/keVee, in agreement with the $^{83}Kr^{m}$ calibration. This agreement provides confidence that we can trust the ^{22}Na calibration for the data taken before the the $^{83}Kr^{m}$ source became available.

As will be discussed in Sec. II F, the signal yield was not stable throughout the course of the run; the largest signal yield observed in this study was (3.5 ± 0.4) photoelectrons/keVee, a factor of about 3.5 larger than we achieved in our previous measurement (0.9 photoelectrons/keVee [6]). We attribute the increase to immersing the PMTs in the liquid instead of viewing through pressure windows, improved photocathode coverage, and a change in the thickness of the wavelength shifter.

F. Detector stability

The presence of impurities can reduce the amount of light detected both by quenching excimer states nonradiatively or by absorbing scintillation light, and both processes have been studied in liquid argon [29–31]. We monitored both the light yield and the triplet lifetime over the course of the experiment to gauge the effect of impurities. Initially, the signal yield of the detector was only 1.9 photoelectrons/keVee. We then engaged the circulation pump and flowed neon through the charcoal trap shown in the schematic of Fig. 2 to remove impurities. The light yield subsequently increased, reaching a peak at (3.5 ± 0.4) photoelectrons/keVee as shown in Fig. 8, providing evidence that impurities were being contained by the charcoal. Because we could not purge the internal charcoal trap while running the experiment, it is not clear whether all the impurities in the neon were removed or whether the trap became saturated. These data were taken for a liquid temperature of 28.7 K.

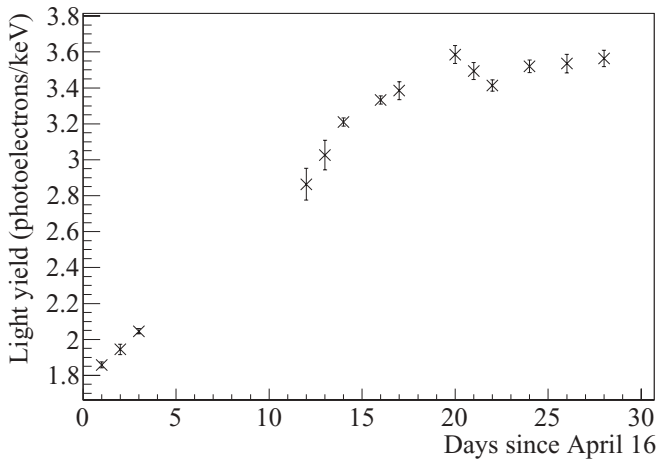

FIG. 8. The light yield in the detector as a function of time with the circulation pump to the charcoal trap engaged for a liquid temperature of 28.7 K as determined by the ^{22}Na source. The light yield reached a maximum at (3.5 ± 0.4) photoelectrons/keVee. The error bars are statistical only and do not include the uncertainty introduced by the single-photoelectron response of the bottom PMT.

Both the light yield and the triplet lifetime varied with time. As will be discussed in Sec. V, both of these parameters are strongly and unexpectedly affected by the temperature and pressure of the liquid neon. To stabilize the temperature and pressure, we disengaged the circulation pump for the remainder of the run, potentially allowing contaminants to build up in the neon and decreasing the observed light yield in the $^{83}Kr^{m}$ data taken at the very end of the experiment to the (3.0 ± 0.3) photoelectrons/keVee reported above.

To account for the temperature effects, the PSD and $\mathcal{L}_{\rm eff}$ data were collected at three different temperatures, 26.7, 27.8, and 28.7 K, where each data set was taken over a roughly two-week period. We measured the light yield approximately every other day during each run to determine the stability of the detector for each temperature set point. The observed signal yields were 2.74 ± 0.03, 3.15 ± 0.08, and 3.13 ± 0.03 photoelectrons/keVee at 26.7, 27.8, and 28.7 K respectively, where the error bars represent the root-mean-square error of all the calibration runs taken at the operating temperature. We therefore conclude that the detector signal yield was stable to better than 3% for each temperature setting.

III. PULSE SHAPE DISCRIMINATION

We define the prompt fraction f_p as

$$f_p = \frac{\int_{T_i}^{\xi} V(t)\,dt}{\int_{T_i}^{T_f} V(t)\,dt}, \tag{5}$$

where $V(t)$ is the voltage trace from the PMT, $\xi = 220$ ns is an integration period determined to optimize the PSD [6], $T_i = t_0 - 50$ ns, $T_f = t_0 + 44\ \mu$s, and t_0 is the trigger time. As mentioned in the previous section, we collected data at 26.7, 27.8, and 28.8 K. In energy bins of 5 keVee, we fit a Gaussian function to the empirical distributions to determine the mean prompt fraction, $\hat{f}_p$, for nuclear and electronic recoils, and Fig. 9 shows $\hat{f}_p$ as a function of energy for both classes of events. The error bars include both statistical uncertainties and a systematic uncertainty of 2.5% stemming from differences in the two PMTs, with the systematic error generally dominating; the total uncertainty is smaller than the size of the markers for the electronic recoil data. There is also a small systematic error associated with fitting an asymmetric distribution with a symmetric Gaussian function that we do not include in this analysis. The nuclear recoil data were acquired in coincidence with a BC501A organic scintillator module as described in Sec. II B. Two effects may be observed: first, the mean prompt fractions for nuclear and electronic recoils converge at low energies. This effect has been observed in liquid argon [9,10] and is likely because dE/dx curves for nuclear and electronic recoils also converge as the energy decreases. Also, the mean prompt fraction decreases with increasing temperature and pressure for both electronic and nuclear recoils at all energies. This will be discussed further in Sec. V.

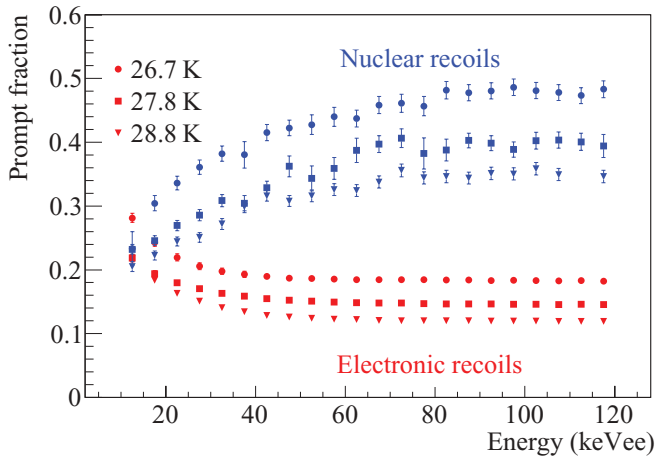

FIG. 9. (Color online) Mean prompt fraction as a function of energy for electronic and nuclear recoils at three different temperatures. The error bars include both statistical and systematic uncertainties and are generally dominated by a 2.5% uncertainty stemming from differences in the two PMTs.

We define the electronic recoil contamination (ERC) as the probability of mistaking an electronic recoil for a nuclear recoil given a particular level of nuclear recoil acceptance. We estimate the ERC as the number of tagged electronic recoil events with $f_p > \hat{f}_{p,\text{nuclear}}$, setting the nuclear recoil acceptance level to approximately 50%. The observed ERC at each temperature is shown in Fig. 10. Our observed ERC is about a factor of 5–10 better than that observed in [6]. Theoretically, we might have expected a stronger improvement given that we collect at least three times as much light. The smaller than expected improvement is in part attributable to the use of a $\hat{f}_{p,\text{nuclear}}$ that changes with energy, instead of the flat-cut value assumed previously in [6]. As shown in Fig. 9, the mean prompt fractions for electronic and nuclear recoils converge at lower energies, reducing the discrimination power.

A second cause of weak PSD is the electronic noise in the experiment. We fit the data using a statistical model for

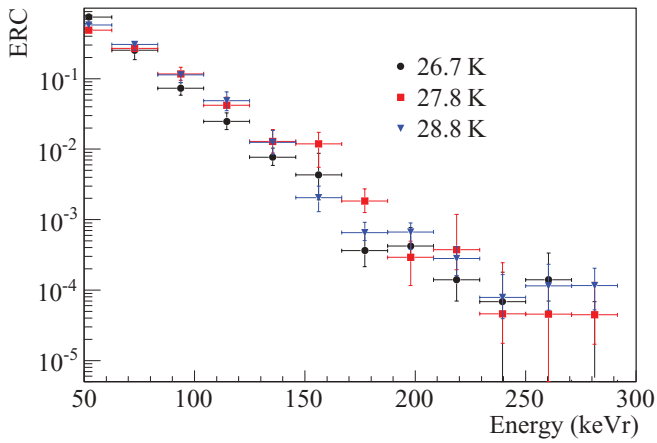

FIG. 10. (Color online) ERC vs energy for the three data sets. The x axis is given in relevant units for dark matter searches, keVr, by assuming $\mathcal{L}_{\text{eff}} = 0.24$ (see Sec. 4).

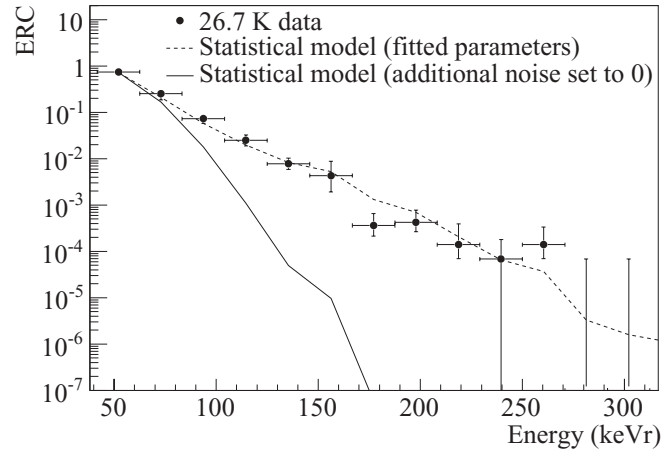

FIG. 11. PSD for the 26.7 K data set individually, along with a fit to the statistical model. The solid line shows the model prediction with additional noise terms set to zero. We note that the effect of the additional noise is most relevant for energies above 100 keVr.

f_p described in [9,10], and Fig. 11 shows the PSD for the 26.7 K data with a fit to this model. In [9], we described a method for estimating the size of the additional noise for comparison between detectors, modeling the prompt and late noise as a constant multiplied by the mean prompt and late signals: $\sigma_p^2 = C_p \mu_p$ and $\sigma_l^2 = C_l \mu_l$. As discussed in [9], we are wary of interpreting these fit parameters as a literal measurement of the noise; however, we do believe they can be used as points of comparison. With that method, the noise parameters in the liquid neon are a factor of 2–3 larger than those observed in argon. The probable cause for such a large amount of noise is the poor gain characteristics of the PMTs and the use of an additional amplifier physically far away from the PMT itself, in addition to the factor of 4 longer integration period required for liquid neon scintillation. The solid line in Fig. 11 shows the statistical model prediction in the ideal case where the additional noise is set to zero. We note that the effect of the additional noise is most relevant for energies above 100 keVr.

To test the hypothesis that the poor PMT response negatively affected the PSD results, the signals in each PMT were analyzed separately. As expected given the single-photoelectron distributions, the bottom PMT provided as much as an order of magnitude better PSD compared to the top PMT above 150 keVr, dropping to a factor of about 2 at lower energies, although the combination of the two PMTs still provides an improvement over just the bottom PMT alone. To achieve better overall PSD, more effort will be needed to improve the response of the PMTs at liquid neon temperatures; as the two PMTs exhibited different behaviors when cold, all PMTs intended for use in a liquid neon detector may need to be cryogenically tested. Another potential area of improvement would be a more sophisticated discrimination statistic. Given the complicated nature of scintillation in liquid neon (see Sec. V), a PSD analysis using more of the timing information along the lines of the multibin method described in [9] might prove rewarding.

IV. NUCLEAR RECOIL SCINTILLATION EFFICIENCY

As mentioned in Sec. I, it is well known that nuclear recoils produce less scintillation light in liquid noble gases than electronic recoils do. There are several processes related to the linear energy transfer (LET) of the incoming radiation that are known to contribute to the lower scintillation efficiency of nuclear recoils. The first of these is the Lindhard effect [32], where some of the energy deposited goes into heat instead of the creation of molecules. The Lindhard effect has been shown to be sufficient to explain quenching in germanium [33], but it is inadequate to explain $\mathcal{L}_{\rm eff}$ for the noble gases. A second mechanism is known as bi-excitonic or Hitachi quenching [34], whereby

$$\mathrm{Ne}^* + \mathrm{Ne}^* \rightarrow \mathrm{Ne} + \mathrm{Ne}^+ + e^-. \quad (6)$$

When such a reaction occurs, the potential for creating two photons from the two original exciton states has been reduced to one photon via recombination of the single resulting ion. This reaction is more likely to occur in high-density tracks like those produced by nuclear recoils. Recently, a model has been proposed to phenomenologically tie this quenching to the stopping power [19,35]. Lastly, some fraction of ionized electrons never recombine; if these "escape electrons" are more likely for nuclear recoils than electronic recoils, this process would contribute to a smaller $\mathcal{L}_{\rm eff}$. This effect has been observed to lower $\mathcal{L}_{\rm eff}$ in liquid xenon [19,36,37].

The experimental setup for measuring the nuclear recoil scintillation efficiency has been described in [15] in the context of a measurement in liquid argon. One salient difference between the current analysis and the argon analysis is the absence of MC simulations of the neutron scattering. There are few experimental data on neon-neutron scattering, with GEANT4 switching discretely from data to a model for neutrons of energy $<$20 MeV. There are efforts underway to improve this situation for future studies [38].

Instead of fitting MC spectra to the data to determine the scintillation efficiency, a simple Gaussian function is fit to the data to determine the mean of the observed peak in units of keVee. Given the non-Gaussian nature of the single-photoelectron distribution, we expect some skewing of the observed spectra toward high energies. In a simple MC of a similar situation in a larger detector, the contribution of this skew is $\approx 5\%$ for the lowest energy point, below the level of our dominant uncertainties. Hence, our scientific judgment is that the uncertainty introduced by this skew does not contribute significantly to our final uncertainty estimate. The final expression for $\mathcal{L}_{\rm eff}$ is the observed mean of the signal yield divided by the expected energy of the recoil as predicted by Eq. (3).

Data were taken at nine different scattering angles corresponding to energies ranging from 28.9 to 368.7 keVr. Each point, with the exception of the point at 178 keVr, was taken at the three different operating temperatures. The results at each temperature are consistent with each other to within the uncertainties of the measurement, so for the final determination of $\mathcal{L}_{\rm eff}$, all the data from each temperature are combined into one data set. Figure 12 shows the final Gaussian fits at each energy, and Fig. 13 shows the observed nuclear recoil scintillation efficiency, along with the result from the previous measurement at 387 keVr [6]. To obtain $\mathcal{L}_{\rm eff}$ we assume that the signal yield from electronic recoils scales linearly with energy (consistent with our observations between 40 and 511 keVee) and compare it to the corresponding signal yield at each nuclear recoil energy. The mean value of $\mathcal{L}_{\rm eff}$ thus obtained is 0.24.

Because we expect there to be some contamination from multiple-scattering and γ backgrounds into the distribution, as observed in argon data [15], we limit the fit range in the region of the peak in the distribution; the fit range is iteratively chosen to encompass $\pm 1\sigma$ from the central value representing our estimate of the mean energy of the peak. The uncertainty associated with this choice of fit range will be discussed in Sec. IV B. The average χ^2/NDF for the fits shown in Fig. 12 is 1.07; the largest value of χ^2/NDF is 2.5 for the 132.2-keVr peak, with all others below 1.3.

A. Data selection cuts

One data selection cut requires that the two PMTs trigger within 40 ns of each other and that the asymmetry parameter is within 1σ of the mean asymmetry value for the run. To select neutronlike events, a PSD cut was applied to the organic scintillator data as shown in Fig. 14. We also apply a TOF cut between an event in the neon and the tagging event in the organic scintillator. A final cut is applied based on the PSD described in the previous section; this is a very loose cut, eliminating events farther than 2σ from the measured mean value of $\hat{f}_p$, for nuclear recoils at 26.7 K.

The TOF cut appears to be quite effective in selecting single-scatter nuclear recoil events in liquid neon. For all runs, neutron events formed a clear peak in the TOF spectrum. As single-scattering neutrons are more likely to be found at the very beginning of the TOF peak, the TOF cut was located at the front side of the peak. First, the total number of counts in the neutron peak was found, and then the TOF distribution was scanned until the number of counts in a 4-ns-wide bin exceeded 3% of the total integral of the neutron peak; this point set the left boundary of the TOF window. The width of the TOF acceptance window was chosen to be 10 ns. An example of the TOF cut is shown in Fig. 15 for 368.7-keV events.

Figures 16 and 17 show the change in the observed energy spectra produced by sliding the location of the TOF cut window to earlier and later times for both the lowest and highest energy runs. If the window is moved 10 ns earlier, very few events pass the cut and no peak in energy is visible. At the standard cut location, clear peaks in the energy spectra for both the low-energy and high-energy points are visible. As the window moves to accept events with longer times of flight, the energy peak loses definition due to the inclusion of multiple-scattering backgrounds, becoming an almost flat background when the TOF cut is moved to the center of the TOF peak (at 20 ns beyond the standard cut). These results provide confidence that the standard TOF cut at the front side of the TOF peak is selecting single-scattering events and eliminating multiple-scattering backgrounds.

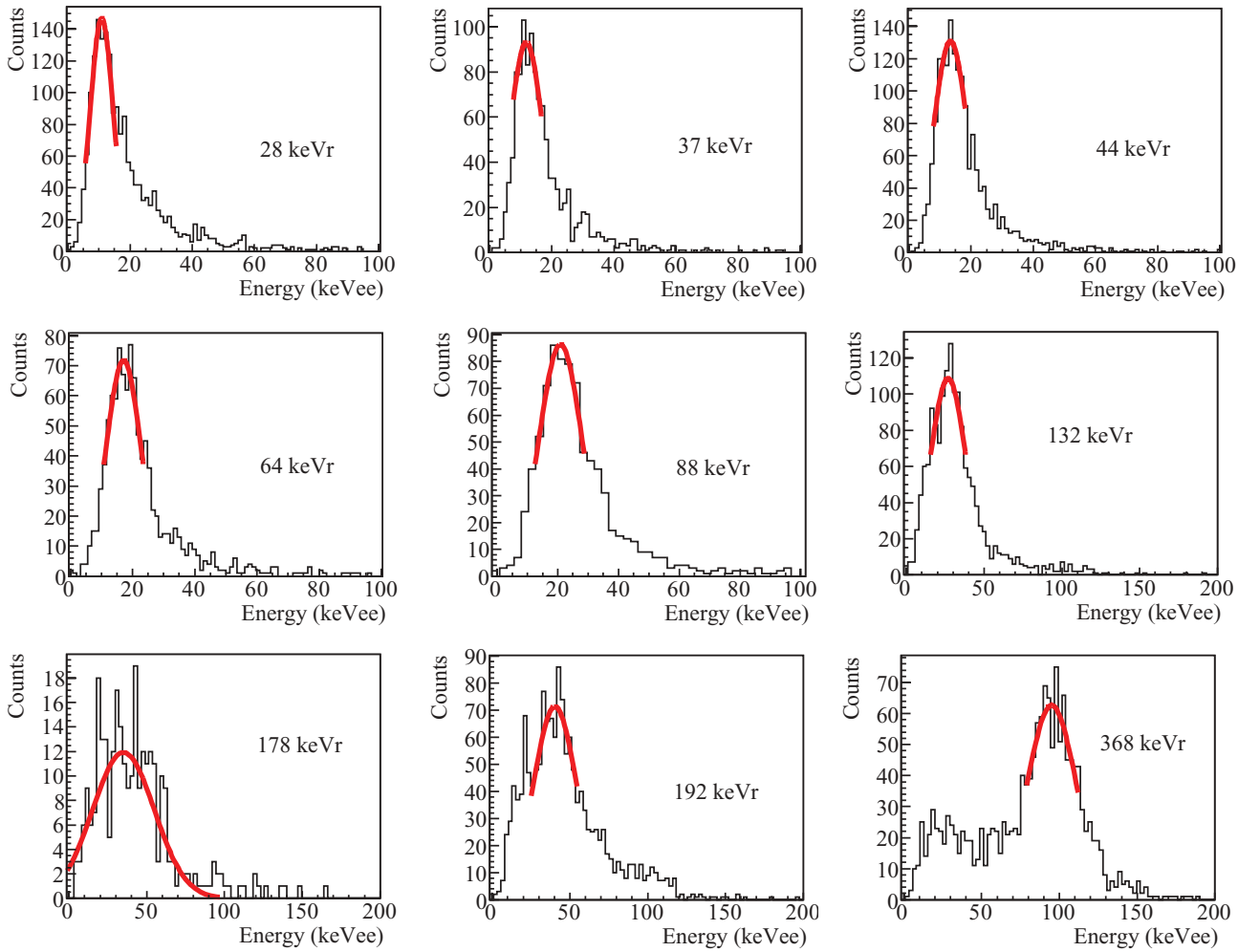

FIG. 12. (Color online) Fits for the nuclear recoil scintillation efficiency in liquid neon for all energies. All data sets include results from each temperature setting, except for the data at 178 keVr that were only taken at 26.7 K.

B. Error analysis

There are a number of sources of uncertainty in this measurement of $\mathcal{L}_{\text{eff}}$ relating to both experimental parameters as well as data selection cuts. There is a general uncertainty of 3% from the energy calibration described above. Studies of the analysis cuts were performed independently to assess the

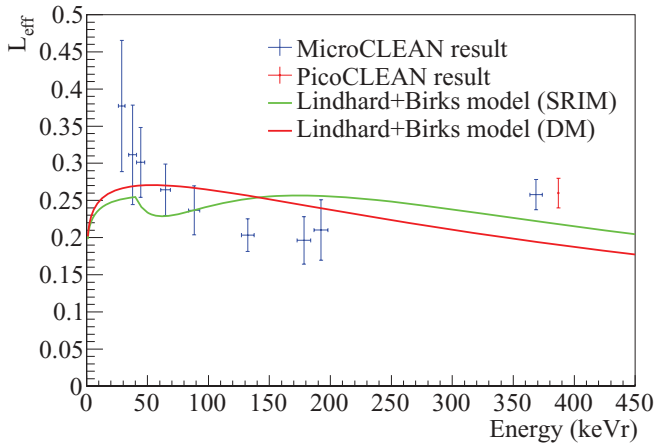

FIG. 13. (Color online) The observed nuclear recoil scintillation efficiency vs nuclear recoil energy in neon, along with the Lindhard + Birks model described in the text.

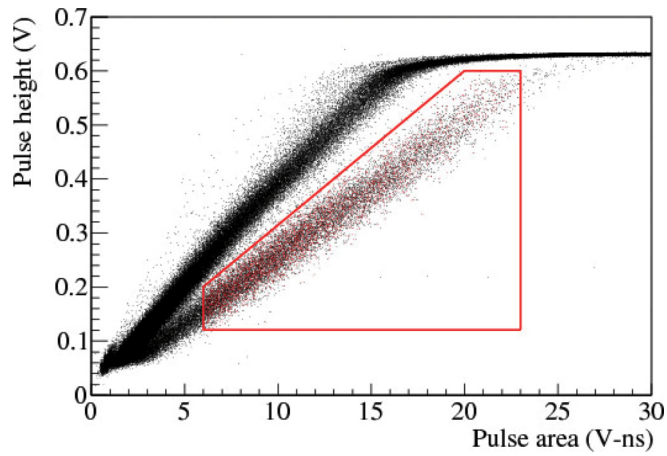

FIG. 14. (Color online) The PSD cut in the organic scintillator to select neutron events. Only events within the pentagon are included in the data set.

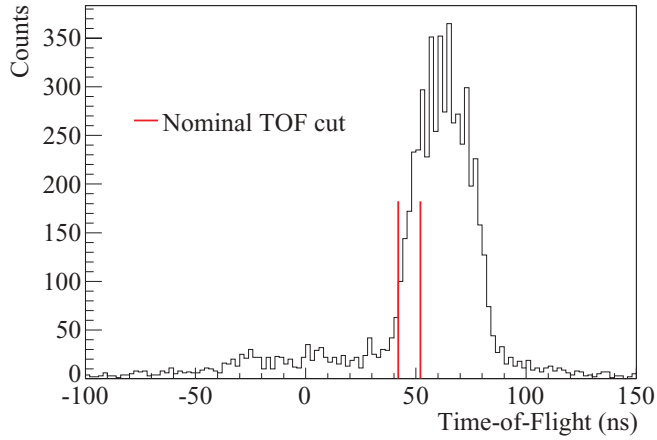

FIG. 15. (Color online) A sample TOF cut. The TOF cut window was 10 ns, and only events at the beginning of the TOF peak were selected, as these events are more likely to be single-scatter events.

size of the systematic error associated with each. In each case, we took the difference between the value of $\mathcal{L}_{\text{eff}}$ determined by the standard analysis and that determined with the changed cut value as our estimate of the systematic error associated with that cut. The size of the coincidence window between the trigger times of the two PMTs was narrowed to 20 ns, and the cut was dropped entirely to study its effect. Both the individual trigger cuts and the asymmetry cut were expanded to encompass the region within 2σ of the mean for the entire run. The range in pulse area of the organic scintillator PSD cut was first narrowed and then scanned across the entire distribution of nuclear recoils (the lower band in Fig. 14). To assess the uncertainty associated with the TOF cut, the width of the TOF window was both narrowed to 6 ns and expanded

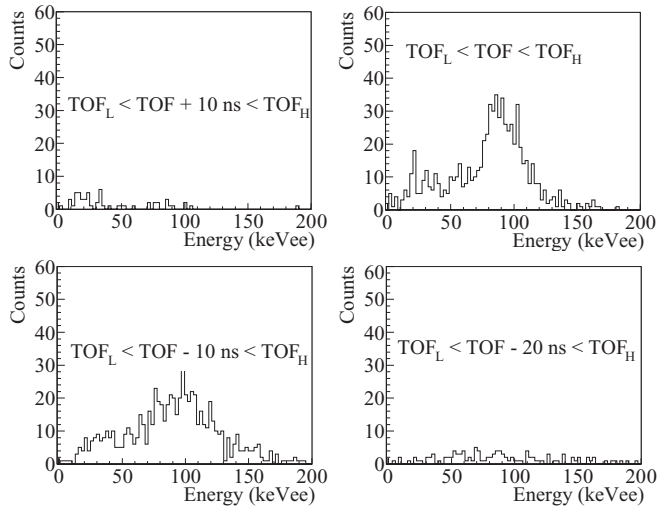

FIG. 16. The observed energy spectrum for 368.7-keVr events as the location of the TOF cut (as defined by TOF_L and TOF_H) is moved by ± 10 and $+20$ ns. The nominal cut around the front side of the TOF peak is the case where $\text{TOF}_\text{L} < \text{TOF} < \text{TOF}_\text{H}$. The degradation in the observed peak as the TOF cut moves away from standard location is clear.

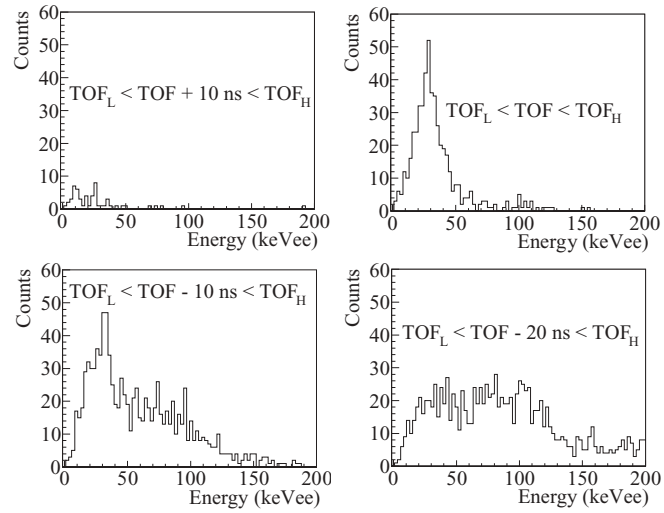

FIG. 17. The observed energy spectrum for 28.9-keVr events as the location of the TOF cut (as defined by TOF_L and TOF_H) is moved by ± 10 and $+20$ ns. The nominal cut around the front side of the TOF peak is the case where $\text{TOF}_\text{L} < \text{TOF} < \text{TOF}_\text{H}$. The degradation in the observed peak as the TOF cut moves away from standard location is clear.

to 16 ns, without changing the location; as already discussed, moving the TOF cut window away from the front of the TOF peak eliminated any observable peak, so the location of the cut was not included as a systematic uncertainty. Finally, the analysis was repeated with no PSD cut applied to the neon data. To estimate the size of the uncertainty associated with the fit range in Fig. 12, the range was expanded to include the region within 2σ of the central value. A source of uncorrelated error is uncertainty in the location of the organic scintillator affecting the predicted value of the nuclear recoil energy. An uncertainty of 0.64 cm in the location of the organic scintillator around the detector corresponds to an angular uncertainty of 1.3° at each position. A final source of uncertainty is the trigger efficiency. Data for the three lowest energy positions were taken at different hardware trigger thresholds such that the difference between the lowest and highest threshold was larger than the average height of a single photoelectron in each PMT.

The statistical uncertainties in the fit results of Fig. 12 were generally below the level of the other uncertainties in the measurement. The main source of uncertainty for the lower energies found in the experiment was the choice of fit range, producing an uncertainty of as large as 15% in the 28.9-keVr data set. In all cases, the effect of increasing the fit range was to increase the observed value of $\mathcal{L}_{\text{eff}}$. The results from changing the hardware threshold were consistent with each other at each of the lowest three energy points. At the highest energies, the dominant source of uncertainty was the width of the TOF window. All sources of uncertainty were assumed to be independent and combined in quadrature to produce the final uncertainty values shown in Fig. 13. Table I lists the central values and the uncertainties associated with each identified source of error.

TABLE I. The observed $\mathcal{L}_{\text{eff}}$ parameters as a function of energy along with the estimated uncertainties for each of the sources of uncertainty listed in the text. The "Fit range" column refers to expanding the fit range out to 2σ. The hardware threshold was varied for only the three lowest energy points. The "OSc cut" column refers to the location of the data cut used on the organic scintillator neutron detector. "TOF size" refers to the size of the time-of-flight cut, which was both expanded to 16 ns and shortened to 6 ns, with both contributions included in that column. The "Temp." column lists the standard deviation of the three temperature set points. All uncertainties that did not contribute at the hundredths level have been listed as zero.

Energy	$\mathcal{L}_{\text{eff}}$	Systematic uncertainty													
(keV)		ΔE (keV)	Energy calib.	Fit range	Relative trigger	Absolute trigger	Hardware threshold	OSc cut	Asym.	f_p cut	TOF size	Temp. (σ)	Total sys.	Stat. uncert.	Total uncert.
29	0.38	2	0.01	0.06	0.01	0.01	0.03	0	0.01	0.01	0.02	0.02	0.08	0.04	0.09
38	0.31	3	0.01	0.04	0.02	0.02	0.01	0.02	0.01	0.02	0.02	0.01	0.06	0.03	0.07
44	0.30	3	0.01	0.02	0.01	0.01	0.02	0.01	0.01	0	0.01	0.02	0.04	0.03	0.05
65	0.26	4	0.01	0.01	0.02	0.01	–	0.02	0	0.01	0.02	0.01	0.03	0.02	0.04
88	0.24	4	0.01	0.02	0.01	0	–	0	0	0	0.02	0.01	0.03	0.01	0.03
132	0.20	5	0.01	0	0.02	0	–	0	0	0	0	0.01	0.02	0.01	0.02
178	0.20	5	0.01	0	0.01	0	–	0.01	0	0	0.02	0	0.03	0.01	0.03
192	0.21	5	0.01	0	0.01	0	–	0	0.01	0	0.03	0.02	0.04	0.01	0.04
369	0.26	5	0.01	0	0	0	–	0	0	0	0.01	0.02	0.02	0	0.02

C. Discussion and the Lindhard + Birks Model

The first point to note about our results for $\mathcal{L}_{\text{eff}}$ in liquid neon is an upturn at low energies similar to one observed in our previous measurement of $\mathcal{L}_{\text{eff}}$ in liquid argon [15], although the uncertainties on the lowest energy points are also the most significant. Both hardware and software trigger effects were examined in attempts to explain this upturn, with neither producing the observed result. As with argon, we do not know whether this is a physically real effect.

In Sec. I, two main processes were listed as causes of the lower scintillation efficiency of nuclear recoils in liquid noble gases. The first was the Lindhard effect, where some energy goes into heat instead of the creation of molecules. A second effect was Hitachi quenching, where two excited atomic states interact to produce one ground-state atom and one ion, reducing the total number of Ne_2 molecules available to produce scintillation photons. Mei *et al*. have developed a phenomenological model to account for these two effects [35], and we apply that model here to the current results drawing values for the stopping power from the tables of SRIM [39] ("SRIM" in Fig. 13). We also use stopping powers obtained from Mei *et al*. from a second model for stopping power as described in [35] ("DM" in Fig. 13).

The result of fitting the Lindhard + Birks model to our data is shown in Fig. 13. The Birks parameters, kB, for the SRIM and DM stopping powers are determined to be 1.99×10^{-3} and 1.73×10^{-3} MeV^{-1} g cm^{-2}, respectively. This can be compared to the value of 1.12×10^{-3} MeV^{-1} g cm^{-2} determined in [35] from the single data point marked as "PicoCLEAN result" in Fig. 13. The kink that appears around 40 keVr in the SRIM curve is potentially mirrored in the upturn at low energies but is not present in the DM model. In developing the Lindhard + Birks model for argon, Mei *et al*. found a similar kink from the SRIM data that was not present in alternative models [35].

V. SCINTILLATION TIME DEPENDENCE

The established model for scintillation in liquefied noble gases consists of two exponentially decaying components representing the contribution from singlet and triplet molecules. In our measurements of scintillation in liquid neon, although fast and slow exponential behavior is observed, neither a two-component nor a three-component model is sufficient to describe the time dependence. In addition, the observed time constants and intensities of each component vary significantly with the temperature and pressure of the liquid. In an attempt to understand the various components of liquid neon scintillation and the temperature dependence, we examine average traces from electronic recoil events with energies between 300 and 400 keVee for nine different pressure and temperature settings. All data are derived from tagged ^{22}Na events; the trigger times of each event in the data sets are aligned and the events are summed together to produce the average traces.

Figure 18 shows an example trace for data taken at 27.4 K, along with fits to two- and three-exponential models. While the three-exponential model improves on the quality of the overall fit, it still does not accurately model the data between about 50 ns and 1 μs. We therefore adopt a four-exponential mixture model [40]. The exponential decay constants are denoted τ_i, and the relative weights, which are non-negative and sum to 1, are denoted I_i. The mixture model for the probability density function (PDF) of the creation times of scintillation photons created by an energy deposition at $t = 0$ is

$$f(t) = \sum_{i=1}^{4} \frac{I_i}{\tau_i} e^{-t/\tau_i}. \tag{7}$$

We model the expected voltage trace produced by the PMTs as a convolution of an experimentally determined impulse response function of the PMT, $h(t)$, and the PDF model:

$$\langle V(t) \rangle \propto \int_{t_0}^{t} h(t-s) f(s-t_0) ds, \tag{8}$$

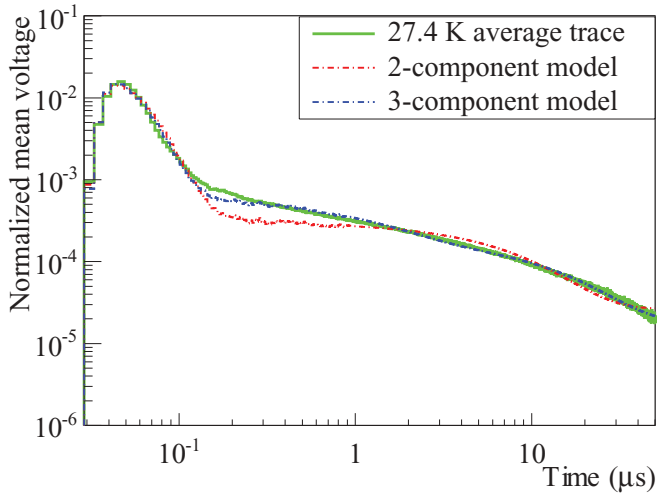

FIG. 18. (Color online) The average traces for 27.4 K data, along with fits to two-component and three-component exponential models. Neither model accurately describes the intermediate time regime.

where t_0 is the time of the energy deposit. We perform the fit by minimizing the Matusita distance [41] between the model and the data.

Example fits to the 26.7 and 28.8 K data are shown in Fig. 19. We associate τ_1 and τ_2 with the longest and shortest time components of the scintillation, respectively, and they are shown in Fig. 20 as a function of neon temperature. The short time constant, τ_2, should not be strictly associated with the decay of the singlet state, as the fast component is also affected by the timing characteristics of the TPB wavelength shifter and the PMTs. The remaining scintillation time constants, representing intermediate time scales, are shown in Fig. 21.

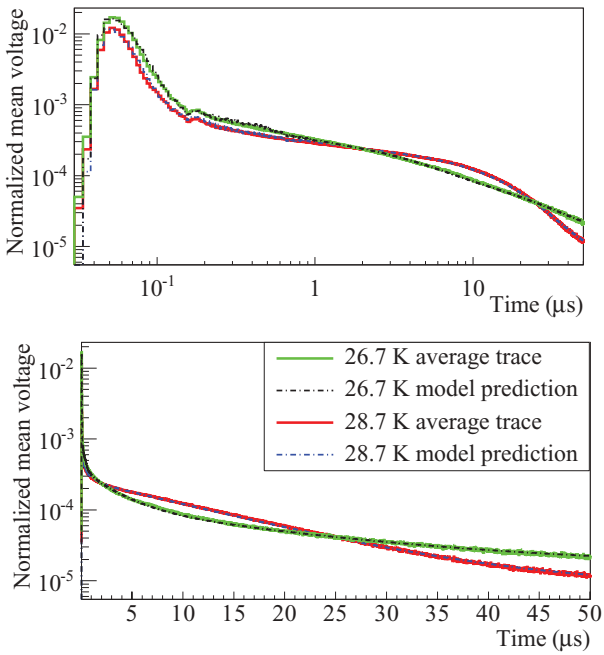

FIG. 19. (Color online) Examples of the four-component model fit to 26.7 and 28.8 K data.

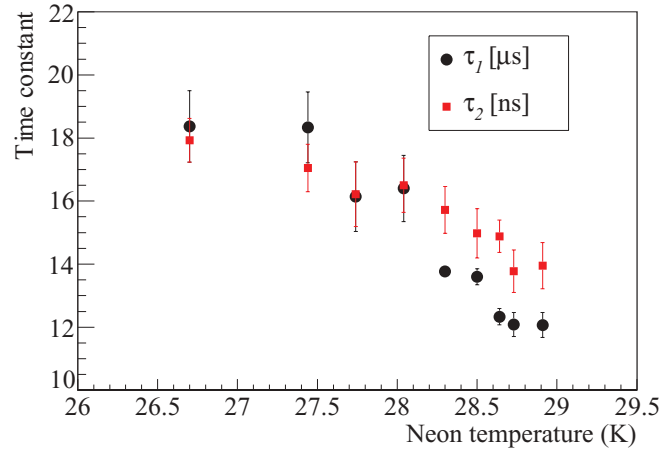

FIG. 20. (Color online) The fitted longest and shortest time constants, τ_1 and τ_2, for neon scintillation as a function of neon temperature. The error bars represent the combined estimated statistical and systematic uncertainties, derived as described in the text.

The weights of each component as a function of temperature are shown in Fig. 22, and all fit parameters are reported in Table II.

We estimate 1σ random uncertainties using a bootstrap resampling scheme [42]. We determine approximate estimates of the systematic uncertainties associated with choice of fit window by varying the end time of the integral in Eq. (8) between 44 and 52 μs. We estimate the systematic uncertainty associated with our measurement of the single-photoelectron response of the PMTs by using several different estimates of $h(t)$ taken from different data sets throughout the run. We also perform the fit for each PMT individually to estimate the uncertainties associated with the different PMTs. In Figs. 20–22, the error bars represent the combination in quadrature of the statistical and systematic uncertainties. In many cases, the error bars are smaller than the size of the marker. As a further consistency check, the analysis was repeated for events with

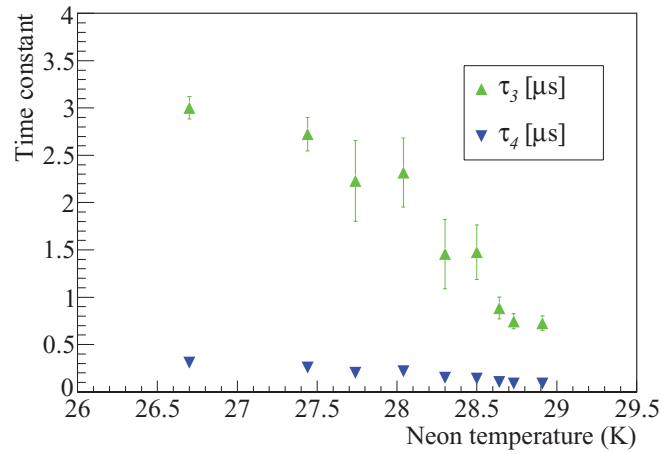

FIG. 21. (Color online) The fitted intermediate time constants, τ_3 and τ_4, for neon scintillation as a function of neon temperature. The error bars represent the combined estimated statistical and systematic uncertainties, derived as described in the text.

TABLE II. Estimated time dependence parameters of the four-exponential model for scintillation in liquid neon. The long and short components are τ_1 and τ_2, respectively, and the intermediate components are τ_3 and τ_4. I_i represents the relative weight of each component.

T	p	τ_1	σ_{τ_1}	τ_2	σ_{τ_2}	τ_3	σ_{τ_3}	τ_4	σ_{τ_4}	I_1	σ_{I_1}	I_2	σ_{I_2}	I_3	σ_{I_3}	I_4	σ_{I_4}
(K)	(mbars)	(μs)		(ns)		(μs)		(μs)									
Electronic recoils																	
26.7	816	18.37	1.13	17.93	0.70	3.00	0.12	0.31	0.03	0.56	0.02	0.16	0.01	0.23	0.02	0.049	0.002
27.4	1048	18.34	1.12	17.05	0.75	2.72	0.18	0.26	0.03	0.66	0.02	0.13	0.01	0.17	0.02	0.039	0.003
27.7	1160	16.14	1.10	16.22	1.02	2.23	0.43	0.20	0.04	0.73	0.03	0.11	0.01	0.12	0.02	0.032	0.004
28.0	1281	16.40	1.05	16.50	0.86	2.32	0.36	0.22	0.04	0.71	0.03	0.12	0.01	0.13	0.02	0.034	0.004
28.3	1380	13.77	0.15	15.72	0.74	1.46	0.37	0.15	0.02	0.81	0.02	0.097	0.005	0.07	0.01	0.025	0.004
28.5	1467	13.60	0.25	14.97	0.78	1.48	0.29	0.14	0.02	0.81	0.02	0.10	0.01	0.07	0.01	0.025	0.003
28.6	1520	12.33	0.26	14.88	0.51	0.89	0.12	0.10	0.01	0.85	0.01	0.089	0.004	0.04	0.01	0.020	0.002
28.7	1575	12.09	0.38	13.77	0.67	0.75	0.08	0.09	0.01	0.86	0.01	0.08	0.01	0.037	0.004	0.020	0.002
28.9	1662	12.07	0.39	13.95	0.73	0.73	0.08	0.09	0.01	0.86	0.01	0.08	0.01	0.035	0.004	0.019	0.002
Nuclear recoils																	
27.7	1160	13.80	0.75	18.38	0.88	2.29	0.34	0.31	0.05	0.43	0.01	0.35	0.01	0.142	0.005	0.08	0.01
28.3	1380	10.99	0.51	17.49	1.02	1.26	0.31	0.175	0.04	0.52	0.02	0.32	0.01	0.105	0.004	0.05	0.01

energy between 50 and 150 keVee, and all the trends discussed below were observed.

We make a few general observations regarding the data before continuing to a discussion of the physics. First, the observed time constants decrease with increasing temperature and pressure (Figs. 20 and 21). Second, the relative intensity of the long-lived component increases with temperature, primarily at the expense of the intermediate components with a small contribution taken from the short-lived part (Fig. 22). The total signal yield also changes with temperature. Figure 23 shows the contribution to the total signal yield by each of the four exponential decay processes in the model ($\lambda_i = I_i \times \lambda_{\text{tot}}$, where λ_{tot} is the total signal yield) at four temperatures taken within three days to minimize the effect of changing detector conditions; the total signal yield increases with increasing temperature, suggesting that not all of the increase in I_1 is due to the decreases in the other components.

There are two final observations that can be made from the data. First, the long time constant is affected by the presence of impurities, as the long time constant at constant temperature increased during the purification cycle described in Sec. II F. Second, we perform a similar analysis on untagged nuclear recoil data at two different temperatures and present the results at the bottom of Table II, although these data are limited by statistics. The parameter trends between the two nuclear recoil data sets are consistent with the electronic recoil data, although the long time constant for nuclear recoil events appears to be 1–2 μs shorter than the corresponding time constant for electronic recoils.

A. Time dependence discussion

Besides the very prompt light produced by the decay of singlet states, there are three additional, distinct scintillation

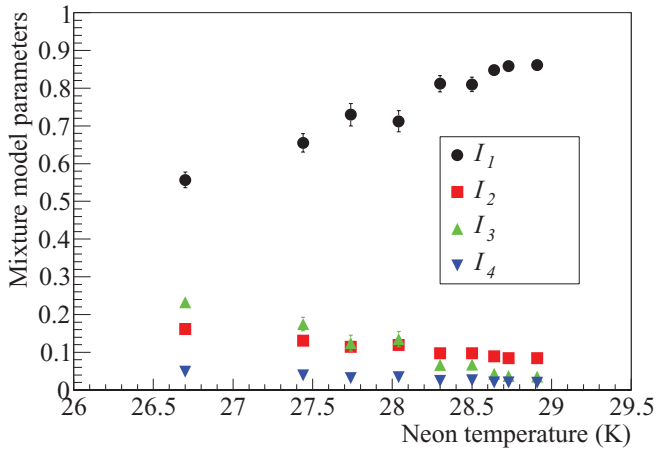

FIG. 22. (Color online) The fitted weights of the four-component model for neon scintillation as a function of neon temperature. The error bars represent the combined estimated statistical and systematic uncertainties, derived as described in the text.

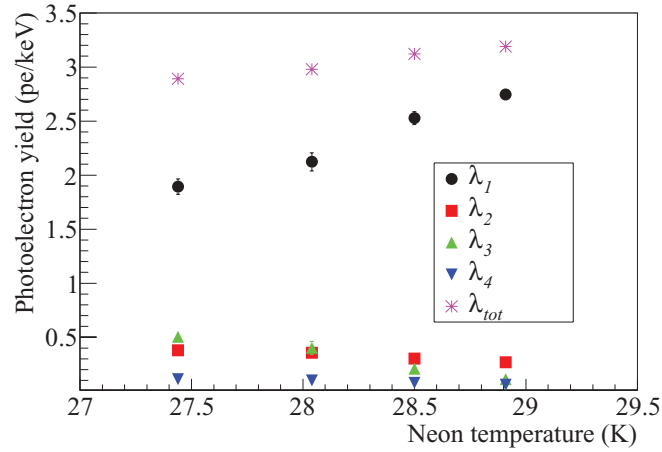

FIG. 23. (Color online) The total signal yield plotted with the intensities of the long, short, intermediate, and residual components as a function of temperature multiplied by the total signal yield of four runs taken over the course of three days.

components. The triplet lifetime in liquid neon has previously been measured to be 15.4, 2.9, and 3.9 μs [6,43,44], with the large discrepancy between the first and second two measurements attributed to impurities in the liquid in the latter two. In solid neon, the long exponential time constant has been measured to be 3.3 and 3.9 μs [43,44]. A very slow tail in the solid has also been observed with a lifetime of 560 μs, attributed to excitations of the $3s^3_{12}P_2$ atomic state [8]; in one measurement of the liquid, an excited atomic triplet state was observed to decay nonexponentially, disappearing within several microseconds [43]. Measurements in gaseous neon suggest that long-lived $^1P_1$ and $^3P_1$ atomic states can react via three-body collisions to form radiative molecular states [45]; the lifetime of the long-lived molecular state in gas, presumably equivalent to the triplet state, was measured to be 6.6 μs [46]. Lastly, as the temperature of the gas is reduced, the emission due to molecular states disappears, leaving only the atomic spectra behind [8].

Before further discussing the current neon data, we compare the results to the situation in argon and helium. First, the data presented in [9] for scintillation in liquid argon were taken at many different temperatures covering a larger absolute temperature range than that examined in liquid neon, and there was no change in the observed triplet lifetime or signal yield in argon.

In liquid helium, the triplet lifetime is 13 s [47]. Two other characteristic time scales were observed in scintillation in liquid helium. First, metastable He(2^3S) atoms created by ionizing radiation have been observed to last for 8000 s in vacuum [48,49]; in liquid, these states only last for 15 μs, and their disappearance is accompanied by the appearance of vibrationally excited triplet molecules, implying the creation of molecules by collisions of the excited atomic states [50]. Second, a t^{-1} component has been observed over a finite time window and attributed to collisions of long-lived triplet states leading to the production of the shorter-lived singlet states which promptly decay [51]. King and Voltz (KV) developed a model to describe slow emission light produced by scintillators via triplet-triplet collisions, neglecting the effects of the radiative decay of triplet molecules [52]. The KV model was adapted by McKinsey *et al.* to describe the t^{-1} component in helium over a finite time window, although the exact form of the power law depends on the assumed track geometry [51].

Finally, an important similarity between liquid helium and liquid neon that sets them apart from the heavier noble gases is that free electrons form bubbles or "localized" states in both liquids [53–57]. These bubble states occur because the electron-atom repulsion due to Pauli exclusion is strong relative to the weak polarization of helium and neon atoms, as evidenced by a positive scattering length for low-energy electrons in helium and neon [58–60]. In the heavier noble gases, the polarization term becomes stronger and overwhelms the repulsive pseudopotential. While electron bubbles would influence recombination rates, affecting the timing of scintillation on short time scales as well as the number density of singlet and triplet molecules, it is unlikely that they are important for the late-time behavior. However, in liquid helium, He_2^* molecules also form bubble states [61–63]. Similar studies and calculations have not been performed for liquid neon, but it is certainly possible that Ne_2^* could also form bubble states, affecting the long-lived triplet molecules and providing another difference between scintillation in liquid neon and liquid argon.

The comparison to liquid helium seems to provide the most illumination, particularly as free electrons form bubbles in both liquids. As in the current measurements, four time components have been observed in liquid helium scintillation: a prompt decay from singlet molecules, a slow exponential decay from triplet molecules, an intermediate exponential decay from atomic states that can also react to form molecules, and a t^{-1} component from triplet molecules reacting to produce singlet molecules.

In neon, we likewise attribute the slowest and fastest (τ_1 and τ_2) components to singlet and triplet molecules. The number of promptly created singlet molecules decreases with increasing temperature and pressure, while the number of triplet molecules greatly increases. We know that there is a connection between the recoil track density and the production of singlet and triplet molecules, and a possible contributor to the changing intensities of each component is the changing density of excitations with temperature. From measurements of the electron mobility and the Einstein relation, the diffusion constant for localized electrons increases by 30% between 26.7 and 28.8 K [53]. Recalling that one channel for the production of metastable molecules is ion-electron recombination, in a simplified picture one expects a larger diffusion constant for electrons to result in a greater maximal separation between ions and recombining electrons. This could produce a greater proportion of triplet molecules given the necessity of an electron spin flip, a mechanism that has been proposed to explain the behavior of xenon scintillation under an electric field [13]. However, the increase in I_1 with increasing temperature is much greater than the corresponding decrease in I_2, requiring some additional explanation that may be found in the intermediate components.

Continuing to examine the triplet states, we must also conclude that the apparent lifetime of the triplet molecules changes as a function of the temperature or pressure of the liquid environment. Impurities in liquid noble gases can shorten the apparent triplet lifetime via absorption or nonradiative collisions. However, in the data of Table II, the shorter lifetime observed at higher temperature and pressure is not accompanied by a decrease in I_1; in fact, the contribution of the triplet component greatly increases with decreasing τ_1, contrary to what one would expect if decreasing τ_1 was caused by impurities.

One possible mechanism that could explain the changing triplet lifetime without an accompanying reduction in I_1 is the presence of molecular bubble states analogous to those found in liquid helium; one could easily imagine that the radiative lifetime of the molecule changes depending on whether or not it resides within a bubble. If Ne_2^* molecules are weakly bound in bubbles at these temperatures, then some fraction of molecules could be localized in bubbles with an additional fraction freely existing in the liquid, leading to the following model for the decay rate of triplet molecules, $d\langle N_t\rangle/dt$:

$$\frac{d\langle N_t\rangle}{dt} = -f(p,T)\frac{\langle N_t\rangle}{\tau_b} - [1-f(p,T)]\frac{\langle N_t\rangle}{\tau_{\bar{b}}}. \qquad (9)$$

Here, $f(p,T)$ is a function of temperature and pressure representing the fraction of molecules contained in bubbles, τ_b is the lifetime of molecules in bubbles, and $\tau_{\bar{b}}$ is the lifetime of molecules outside of bubbles. Although such a model could account for the observed behavior, it is purely speculative given our lack of theoretical guidance for whether neon molecules truly do form stable bubbles.

There are two intermediate components, one with a lifetime of order 100 ns and the other with a lifetime of order 1 μs. We can again draw a parallel to the situation in liquid helium and attribute some of this component to collisions between triplet molecules seeding the creation of singlet molecules that immediately decay as in the King and Voltz theory. However, the KV theory cannot entirely account for the intermediate exponential behavior, even if one modifies the KV model to include the decay of the triplet state. Therefore, we attribute the longer-lived intermediate exponential component to either excited atomic states producing singlet molecules that immediately decay or to the decay of the long-lived atomic states themselves. In the first case, the observed lifetime τ_3 is equivalent to the reaction rate of excited atomic states with ground-state Ne atoms; if this collision rate increases with temperature or pressure (perhaps because of increasing diffusion or bubble fluctuations), the observed lifetime would decrease. In the latter case, τ_3 would be some combination of the true radiative lifetime of the atomic excitation and a quenching reaction. In contrast to the very long lived exponential channel, the decreasing τ_3 *is* accompanied by a decreasing I_3, suggesting the existence of a nonradiative channel. Taking the argument one step further, if we combine the two scenarios with the modification that three-body collisions of excited atomic states create *triplet* molecules, the nonradiative channel could result in the production of triplet molecules and the observed increase in I_1. This interpretation could be consistent with the disappearance of a triplet atomic spectrum over several microseconds as observed by Suemoto and Kanzaki [43].

In the future, understanding the effects of an applied electric field on liquid neon scintillation might illuminate some of the temperature and pressure dependencies observed in this work. A second study that would be useful in assessing whether molecules reside in bubble states would be further laser spectroscopy; in liquid helium, molecular bubbles were first discovered in the absence of wavelength shifts for rovibrational structure in emission spectra of He_2^* between gaseous and liquid helium. These studies could be accompanied by theoretical work on the potential existence of molecular bubbles in liquid neon. Third, the experimental conditions of MicroCLEAN required that the liquid follow the saturation line, rendering it impossible to separate the temperature effects from those associated with pressure. It is likely that bubble interactions depend on the pressure more strongly than on the liquid temperature, and an experiment capable of probing the liquid phase space away from the saturation line and at higher temperatures could prove interesting.

VI. CONCLUSION

In this paper, we have reported measurements of scintillation light. With PMTs immersed directly in liquid neon, we have observed a substantial signal yield of up to (3.5 ± 0.4) photoelectrons/keVee. The observed signal yield is greater than what would be required for a pp-neutrino measurement in CLEAN and much larger than the signal yield assumed in previous simulations of a ton-scale CLEAN detector [2,64]. We have demonstrated the use of activated charcoal as a purifier to remove light-reducing impurities in the liquid. We have quantified the performance of the prompt ratio PSD method for liquid neon by measuring the ERC for a nuclear recoil acceptance probability of approximately 0.5 between 50 and 300 keVr, although we believe our measurement to be an upper limit on the discrimination power achievable with liquid neon due to noise in our system. As in previous studies of liquid argon, we observe a convergence of the f_p parameter at low energies. We have also made a measurement of $\mathcal{L}_{\text{eff}}$ in liquid neon. Finally, we have observed a very interesting time dependence of the scintillation of liquid neon, consisting of four distinct components and a clear temperature and pressure dependence in both intensity and timing.

ACKNOWLEDGMENTS

We gratefully acknowledge Dongming Mei for useful discussion and data on the stopping power of neon. We thank Joshua Klein, Stan Seibert, Franco Giuliani, and Thomas Caldwell for useful discussion and for their work on the RAT simulation package. This work was supported by a grant from the Packard Science and Engineering Program, Yale University, and the US Department of Energy. Computer simulations were supported in part by the facilities and staff of the Yale University Faculty of Arts and Sciences High Performance Computing Center.

[1] D. N. McKinsey and J. M. Doyle, J. Low Temp. Phys. **118**, 153 (2000).
[2] M. G. Boulay, A. Hime, and J. Lidgard, Nucl. Phys. B, Proc. Suppl. **143**, 486 (2005).
[3] D. N. McKinsey and K. J. Coakley, Astropart. Phys. **22**, 355 (2005).
[4] D. McKinsey, Nucl. Phys. B, Proc. Suppl. **173**, 152 (2007).
[5] G. Jungman, M. Kamionkowski, and K. Griest, Phys. Rep. **267**, 195 (1996).
[6] J. A. Nikkel, R. Hasty, W. H. Lippincott, and D. N. McKinsey, Astropart. Phys. **29**, 161 (2008).
[7] M. K. Harrison, W. H. Lippincott, D. N. McKinsey, and J. A. Nikkel, Nucl. Instrum. Methods A **570**, 556 (2006).
[8] R. E. Packard, F. Reif, and C. M. Surko, Phys. Rev. Lett. **25**, 1435 (1970).

[9] W. H. Lippincott, K. J. Coakley, D. Gastler, A. Hime, E. Kearns, D. N. McKinsey, J. A. Nikkel, and L. C. Stonehill, Phys. Rev. C **78**, 035801 (2008).
[10] M. G. Boulay *et al.*, arXiv:0904.2930v1 [astro-ph.IM].
[11] P. Benetti *et al.*, Astropart. Phys. **28**, 495 (2008).
[12] J. V. Dawson *et al.*, Nucl. Instrum. Methods A **545**, 690 (2005).
[13] J. Kwong, P. Brusov, T. Shutt, C. E. Dahl, A. I. Bolozdynya, and A. Bradley, Nucl. Instrum. Methods A **612**, 328 (2010).
[14] K. Ueshima *et al.*, arXiv:1106.2209v1.
[15] D. Gastler, E. Kearns, J. Klein, A. Hime, W. H. Lippincott, D. N. McKinsey, J. A. Nikkel, and S. Seibert, Phys. Rev. C **85**, 065811 (2012).
[16] V. Chepel, V. Solovov, F. Neves, A. Pereira, P. J. Mendes, C. P. Silva, A. Lindote, J. P. da Cunha, M. I. Lopes, and S. Kossionides, Astropart. Phys. **26**, 58 (2006).
[17] E. Aprile, K. L. Giboni, P. Majewski, K. Ni, M. Yamashita, R. Hasty, A. Manzur, and D. N. McKinsey, Phys. Rev. D **72**, 072006 (2005).
[18] E. Aprile, L. Baudis, B. Choi, K. L. Giboni, K. Lim, A. Manalaysay, M. E. Monzani, G. Plante, R. Santorelli, and M. Yamashita, Phys. Rev. C **79**, 045807 (2009).
[19] A. Manzur, A. Curioni, L. Kastens, D. N. McKinsey, K. Ni, and T. Wongjirad, Phys. Rev. C **81**, 025808 (2010).
[20] G. Plante, E. Aprile, R. Budnik, B. Choi, K. L. Giboni, L. W. Goetzke, R. F. Lang, K. E. Lim, and A. J. M. Fernandez, Phys. Rev. C **84**, 045805 (2011).
[21] D. N. McKinsey, C. R. Brome, J. S. Butterworth, R. Golub, K. Habicht, P. R. Huffman, S. K. Lamoreaux, C. E. H. Mattoni, and J. M. Doyle, Nucl. Instrum. Methods B **132**, 351 (1997).
[22] Nupure Corporation, Omni Nupure III, www.nupure.com.
[23] W. H. Lippincott, S. B. Cahn, D. Gastler, L. W. Kastens, E. Kearns, D. N. McKinsey, and J. A. Nikkel, Phys. Rev. C **81**, 045803 (2010).
[24] R. Brun and F. Rademakers, Nucl. Instrum. Methods A **389**, 81 (1997).
[25] J. A. Nikkel, W. H. Lippincott, and D. N. McKinsey, J. Instrum. **2**, P11004 (2007).
[26] Thermo Electron model MP320, www.thermo.com.
[27] Reactor Analysis Tool (RAT), https://deapclean.org/rat/trac/.
[28] S. Agostinelli *et al.*, Nucl. Instrum. Methods A **506**, 250 (2003).
[29] R. Acciarri *et al.*, Nucl. Phys. Proc. Suppl. **197**, 70 (2009).
[30] R. Acciarri *et al.*, J. Instrum. **5**, P05003 (2010).
[31] S. Himi, T. Takahashi, J. Ruan, and S. Kubota, Nucl. Instrum. Methods **203**, 153 (1982).
[32] J. Lindhard, M. Scharff, and H. Schiott, Mat. Fys. Medd. K. Dan. Vidensk. Selsk. **33**, 1 (1963).
[33] A. Benoit *et al.*, Nucl. Instrum. Methods A **577**, 558 (2007).
[34] A. Hitachi, Astropart. Phys. **24**, 247 (2005).
[35] D.-M. Mei, Z.-B. Yin, L. Stonehill, and A. Hime, Astropart. Phys. **30**, 12 (2008).
[36] T. Doke, A. Hitachi, J. Kikuchi, K. Masuda, H. Okada, and E. Shibamura, Jpn. J. Appl. Phys. **41**, 1538 (2002).
[37] P. Sorensen and C. E. Dahl, Phys. Rev. D **83**, 063501 (2011).
[38] S. MacMullin, R. Henning, M. Kidd, W. Tornow, and C. Howell, Bulletin of the APS April Meeting (2010).
[39] J. F. Ziegler, M. D. Ziegler, and J. P. Biersack, *SRIM—The Stopping and Range of Ions in Matter* (Elsevier, New York, 2010).
[40] G. J. McLachlan and D. Peel, *Finite Mixture Models* (Wiley-Interscience, New York, 2000).
[41] K. Matusita, Ann. Inst. Stat. Math. **7**, 67 (1954).
[42] B. Efron and R. Tibshirani, *An Introduction to the Bootstrap* (Chapman and Hall, London, 1994).
[43] T. Suemoto and H. Kanzaki, J. Phys. Soc. Jpn. **46**, 1554 (1979).
[44] R. A. Michniak, R. Alleaume, D. N. McKinsey, and J. M. Doyle, Nucl. Instrum. Methods A **482**, 387 (2002).
[45] P. K. Leichner, Phys. Rev. A **8**, 815 (1973).
[46] T. Oka, K. V. S. R. Rao, J. L. Redpath, and R. F. Firestone, J. Chem. Phys. **61**, 4740 (1974).
[47] D. N. McKinsey, C. R. Brome, J. S. Butterworth, S. N. Dzhosyuk, P. R. Huffman, C. E. H. Mattoni, J. M. Doyle, R. Golub, and K. Habicht, Phys. Rev. A **59**, 200 (1999).
[48] J. W. Keto, F. J. Soley, M. Stockton, and W. A. Fitzsimmons, Phys. Rev. A **10**, 887 (1974).
[49] J. R. Woodworth and H. W. Moos, Phys. Rev. A **12**, 2455 (1975).
[50] A. Köymen, F. C. Tang, X. Zhao, F. B. Dunning, and G. K. Walters, Chem. Phys. Lett. **168**, 405 (1990).
[51] D. N. McKinsey *et al.*, Phys. Rev. A **67**, 062716 (2003).
[52] T. A. King and R. Voltz, Proc. R. Soc. London Ser. A **289**, 424 (1966).
[53] L. Bruschi, G. Mazzi, and M. Santini, Phys. Rev. Lett. **28**, 1504 (1972).
[54] R. J. Loveland, P. G. L. Comber, and W. E. Spear, Phys. Lett. A **39**, 225 (1972).
[55] C. G. Kuper, Phys. Rev. **122**, 1007 (1961).
[56] J. Jortner, N. R. Kestner, S. A. Rice, and M. H. Cohen, J. Chem. Phys. **43**, 2614 (1965).
[57] B. E. Springett, M. H. Cohen, and J. Jortner, Phys. Rev. **159**, 183 (1967).
[58] T. F. O'Malley, Phys. Rev. **130**, 1020 (1963).
[59] B. E. Springett, J. Jortner, and M. H. Cohen, J. Chem. Phys. **48**, 2720 (1968).
[60] T. Miyakawa and D. L. Dexter, Phys. Rev. **184**, 166 (1969).
[61] W. S. Dennis, E. Durbin, W. A. Fitzsimmons, O. Heybey, and G. K. Walters, Phys. Rev. Lett. **23**, 1083 (1969).
[62] J. C. Hill, O. Heybey, and G. K. Walters, Phys. Rev. Lett. **26**, 1213 (1971).
[63] A. P. Hickman and N. F. Lane, Phys. Rev. Lett. **26**, 1216 (1971).
[64] K. J. Coakley and D. N. McKinsey, Nucl. Instrum. Methods A **522**, 504 (2004).